Applied Physics Letters

Betatron-type laser-plasma x-ray sources generated in multi-electron gas targets

Cite as: Appl. Phys. Lett. **118**, 131110 (2021); https://doi.org/10.1063/5.0046184
Submitted: 01 February 2021 • Accepted: 14 March 2021 • Published Online: 31 March 2021

A. Grigoriadis, G. Andrianaki, M. Tatarakis, et al.

Applied Physics Letters ARTICLE scitation.org/journal/apl

Betatron-type laser-plasma x-ray sources generated in multi-electron gas targets

Cite as: Appl. Phys. Lett. **118**, 131110 (2021); doi: 10.1063/5.0046184
Submitted: 1 February 2021 · Accepted: 14 March 2021 ·
Published Online: 31 March 2021

A. Grigoriadis,[1,2] G. Andrianaki,[2,3] M. Tatarakis,[2,4] E. P. Benis,[1,a)] and N. A. Papadogiannis[2,5,a)]

AFFILIATIONS

[1]Department of Physics, University of Ioannina, 45110 Ioannina, Greece
[2]Institute of Plasma Physics and Lasers, Hellenic Mediterranean University Research Centre, 74100 Rethymno, Greece
[3]School of Production Engineering and Management, Technical University of Crete, 73100 Chania, Greece
[4]Department of Electronic Engineering, Hellenic Mediterranean University, 73133 Chania, Greece
[5]Department of Music Technology and Acoustics, Hellenic Mediterranean University, 74133 Rethymno, Greece

[a)]**Authors to whom correspondence should be addressed:** mbenis@uoi.gr and npapadogiannis@hmu.gr

ABSTRACT

Betatron-type laser-plasma x-rays are recorded simultaneously with their corresponding relativistic electron spectra in a laser wakefield acceleration scheme. The role of the multi-electron gas target in the betatron-type x-ray efficient generation is experimentally examined. A proof of principle experimental study shows that by using a multi-electron gas target and appropriately adjusting the pumping laser intensity an increase in betatron-type x-rays efficiency could be achieved. This is attributed to sophisticated control of the type of the electron injection inside the plasma bubble related to the tunneling ionization process occurring after the laser pulse peak. This method depends primarily on the gas target charge state chosen for attaining the ionization injection scheme and could be extended to a wide range of relativistic laser intensities.

The generation of relativistic electrons via the laser wakefield acceleration (LWFA) scheme[1–3] and the associated betaron-type x-ray radiation[4,5] has attracted particular attention over the past two decades.[6,7] Experimental setups offering the option to simultaneously record both the x-rays and the relativistic electrons shed light on the understanding of the underlying physical mechanisms, further promoting the development of these secondary sources as well as their applications.[8–13] Simultaneous x-ray and electrons shot-to-shot measurements have already been initiated in terms of controlling the betatron radiation stability and reproducibility.[14]

A critical parameter in these processes is the selection of the appropriate gas target. Helium has been widely used since its ionization with fs relativistic laser fields is completed well before the laser pulse peak. Then, a clear formation of plasma bubble occurs and electrons entering the bubble via self-injection are accelerated by the plasma wave. Additionally, gases with higher Z numbers as well as gas mixtures have also been reported.[15–17] For the latter cases, a different mechanism of electron injection inside the plasma bubble has been proposed, namely, the direct ionization injection scheme.[18,19] This mechanism enhances the number of electron injection inside the plasma bubble the bubble[20] and thus increases the number of betatron-type x-ray emitters.[21] The ionization injection scheme allows for using relatively low values of laser normalized vector potential amplitude a_0 for efficiently generating betatron-type x-rays.[22] However, systematic studies exploring different multi-electron gas targets in controllable experimental conditions, exploring the role of multi-ionization schemes, have not been reported.

Recently, our team reported experimental results on the identification of the betatron-type x-rays from other various types of x-ray radiation and the observation of directional relativistic quasi-monoenergetic electrons from the interaction of high-power laser pulses with He gas targets.[23] Here, we extend our studies to a systematic investigation based on simultaneous shot-to-shot measurements of relativistic electron spectra and betatron-type x-ray radiation profiles, using He, N_2, Ne, and Ar gas targets. Our goal is to examine the role of the multi-electron targets, rich in multi-ionization potentials, in the bubble formation dynamics and ionization injection features, mapped in the generated x-rays and electron spectra. Our experiments are a proof of principle study of the betatron-type x-rays efficiency by using a multi-electron gas target and appropriately adjusting the pumping laser intensity, exploiting different charge state ionization schemes.

The experiments were performed using the 45 TW fs laser system "Zeus" at the Institute of Plasma Physics & Lasers of the Hellenic Mediterranean University. It is a three-stage amplification fs laser system, manufactured by Amplitude Technologies, that delivers pulses with a maximum energy of 1.3 J, central wavelength at ∼800 nm, and duration of 25 fs, at a repetition rate up to 10 Hz. A secondary beam is delivered by the laser system prior to the third amplification stage at an energy of 10 mJ and pulse duration of 25 fs, used for probing the plasma channel at controlled time delays. The experimental setup is illustrated in Fig. 1(a). The laser beam is focused on the gas jet target by a 1 m focal length off-axis parabolic mirror (f/18), resulting in laser peak intensities of 10^{18}–10^{19} W/cm^2. The secondary relativistic electrons and x-rays emitted within the cone of the electron deflection angle are detected simultaneously in shot-to-shot basis.

The gas flow of the pulsed jet was shaped by an electromagnetic valve (Parker) having a 3 mm diameter nozzle. It was found that gas backing pressures between 35 and 45 bar were optimum for the experimental conditions of this work. The gas density profiles were determined using a Nomarski-type interferometric setup along with an analysis algorithm that were both developed for this purpose. Details of this method will be reported in a forthcoming publication. A typical gas density profile is shown in Fig. 1(b) depicting gas densities on the order of 10^{18} cm^{-3}. A lineout of the profile at a typical experimental distance of 1 mm from the exit of the nozzle is shown in Fig. 1(c). The gas density measurements were used for the estimation of the plasma density taking into consideration the degree of ionization for the various gases used. Additionally, a fs laser shadowgraphy setup was developed in order to image the plasma channel formation in shot-to-shot basis at controllable time delays. A typical shadowgram is shown in Fig. 1(d). In this work, shadowgrams were used for monitoring and controlling the plasma channel characteristics, which are necessary for the effective electron acceleration and betatron-type x-ray generation. The uniformity and stability of the plasma density channel is important for the success of such concept.[24] It should be noted that the number of betatron-type x-ray photons is proportional to the length of the plasma channel since the latter is proportional to the electron acceleration length for the laser intensities used in this work.[16]

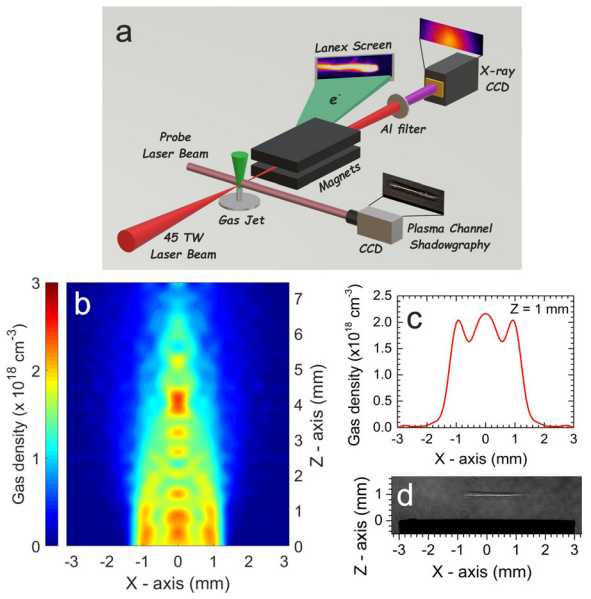

FIG. 1. (a) The experimental setup. The x-rays and relativistic electrons generated by the interaction of the laser pulses with the gas targets are recorded simultaneously in shot-to-shot basis. (b) Typical gas jet density image obtained with a Nomarski-type interferometer. (c) Line out of (b) at distance 1 mm from the jet nozzle showing an almost trapezoidal gas density distribution. (d) Shadowgram of the corresponding to (b) plasma channel obtained from the interaction of the main laser pulse with the gas jet.

The generated x-rays were recorded using a 16-bit x-ray CCD camera (Raptor Photonics, Eagle XO) with a sensor having 2048 × 512 pixels (27.65 mm × 6.90 mm), installed in vacuum at a chamber port 60 cm away from the gas jet. A 10 μm thick Al foil (Goodfellow) was placed in front of the x-ray camera to filter the IR laser beam as well as other secondary light sources in the EUV region. Note that the transmission of EUV radiation (< 500 eV) is lower than 10^{-6} for the 10 μm thick Al foil.[25]

The relativistic electrons were recorded using a home-made magnetic spectrometer consisting of two permanent magnetic plates (11 cm × 9 cm) placed in parallel at a separation distance of 1 cm. The magnetic field was measured with a Hall probe resulting in a homogeneous field ∼0.4 T at its central area. The relativistic electron beam was guided by the magnetic field toward a rectangular (6 cm × 1.5 cm) scintillating screen (Lanex Regular), and the emitted light from the rear side of the scintillating screen was imaged by a lens onto a CCD camera. The electron energy spectra were extracted from the CCD images based on relativistic electron orbit calculations. Considering the magnetic field maximum variations along the central electron trajectory, the measured divergence of the electron beam and the geometry of the setup, the error bar in the energy determination of the electron spectra was estimated to be ∼4%.

In Fig. 2, typical single-shot relativistic electron spectral images (left) and corresponding betatron-type x-ray images (right) recorded simultaneously for He, N_2, Ne, and Ar gas targets are shown.

Initially our study was focused on the He gas, a benchmark gas for LWFA. In Fig. 3, the experimental results for the He gas for two laser pulse energies, 920 mJ (high energy) and 570 mJ (low energy), are presented. Specifically, in Fig. 3(a), the dependence of the x-ray photon number on the electron beam divergence is shown. The photon number was estimated as follows: The x-ray signal was initially encoded in a 2^{16} bit gray color scale signal in our x-ray CCD camera.

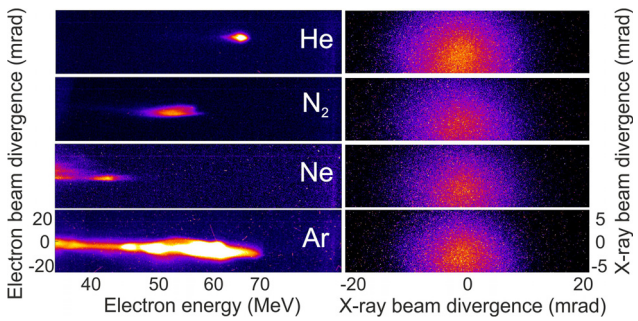

FIG. 2. Typical relativistic electron spectral images (left) and corresponding betatron-type x-ray images (right) recorded simultaneously in single-shot interactions of 570 mJ, 25 fs laser pulses with He, N_2, Ne, and Ar gas targets.

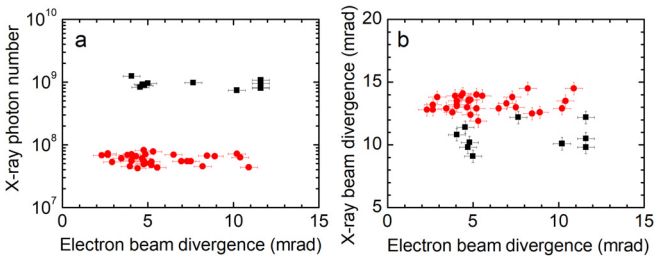

FIG. 3. Experimental results for He gas target obtained with laser pulses having energies of 920 mJ (black solid rectangles) and 570 mJ (red solid circles). (a) X-ray photon number as a function of the electron beam divergence and (b) x-ray beam divergence as a function of electron beam divergence.

The x-ray signal integrated over the sensor area was then subtracted from its background and multiplied by the photo-electron signal to gray-level signal conversion efficiency, given by the manufacturer (1.54 for our CCD camera). Finally, the resulted signal was multiplied by the average quantum efficiency for converging the x-ray light into photo-electron signal, provided by the manufacturer, and by the transmission of the 10 μm thick Al foil.[25] The electron beam divergence corresponds to the half-width half-maximum (HWHM) of the projection of the electron spectrogram along the axis parallel to the magnetic field.

It is evident that while the betatron-type x-rays are relatively insensitive to the electron beam divergence, they strongly depend on the laser pulse energy. From Fig. 3(a), the ratio of the high to low laser energy photon number is estimated 13 ± 1. This difference can be justified as follows: Betatron-type x-ray photon number N_γ depends on the normalized vector potential a_0 as $N_\gamma \sim a_0^{5/2}$, which in our case accounts for a factor of 3.3. Since the normalized vector potentials in use are $a_0 = 1.8$ and $a_0 = 2.3$ for the low and high laser energies, respectively, the linear regime of LWFA is applicable.[16] Therefore, the generated number of photons depends linearly on the acceleration length and thus on the length of the plasma channel. By measuring the plasma channel lengths corresponding to the high and low energies to be 1.9 mm and 1.2 mm, respectively, another factor of 1.6 is estimated. To fully account for the measured ratio, the spectral efficiency detection should be considered as well. However, since our setup does not include an x-ray spectrometer at the moment, we estimated the x-ray spectrum according to well-known formulas of the radiation emitted by a relativistic electron, i.e., synchrotron radiation.[26] The electron beam Lorentz γ factor, necessary for these calculations, was extracted from the measurements of the maximum energy of the electron spectra. The average values of $\gamma = 135$ and $\gamma = 110$ were determined for the high and low laser energies, respectively. The estimated spectra were corrected for the overall detection efficiency and their integrated values resulted in a ratio of 3. Thus, the overall estimated ratio of the high to low laser energy of photon number resulted in 15.8, in fair agreement with the measured value. It should be noted that due to the complete ionization of the He target at the leading edge of the laser pulse, the plasma electron density remains the same for both laser energies.

In Fig. 3(b) the relation of the x-ray beam divergence to the electron beam divergence, also obtained at HWHM, is presented. Note that the divergence of the x-ray beam corresponds only to the long dimension of the sensor of the x-ray CCD camera, while the laser polarization was kept horizontal for all the reported measurements. As it is clearly seen, the electron beam divergence spans a wide-angle distribution between 2 and 12 mrad. The small divergence values typically correspond to the formation of quasi-monoenergetic electron beams while the higher values usually correspond to electron spectra covering an appreciably wider energy window. The x-ray beam divergence shows a much narrower distribution compared to the electron beam divergence, around the values of 13 mrad and 10 mrad for the low and high energies, respectively. Thus, the decrease in the x-ray beam divergence with the laser energy increase is seen as demonstrated from the experimental data of Fig. 3(b). This experimental finding is attributed to the dependence of the x-ray angular divergence θ on the Lorentz factor γ. Specifically, in the wiggler regime, $\theta = K/\gamma$. K defines the undulator and wiggler regimes and is given by $K = 1.33 \times 10^{-10}\sqrt{\gamma\, n_e[\mathrm{cm}^{-3}]}\; r_\beta[\mu\mathrm{m}]$, where n_e is the electron density and r_β is the amplitude of the betatron oscillation that depends on the Lorentz factor γ as[27] $r_\beta \sim \gamma^{-1/4}$. The physical meaning of the decreasing of the oscillation radius is the growth of the relativistic mass and inertia of electrons. Then, the angular divergence of the generated x-ray beam scales as $\theta \sim \gamma^{-3/4}$. Thus, higher laser energies corresponding to higher γ values are expected to result in less divergent x-ray beams, as observed in our data. According to the experimentally determined average γ values of 135 and 110 for the high and low energies, respectively, a reduction 17% of the divergence is expected for the high energy with respect to the low energy, which is in accordance with our experimental findings. Moreover, for $n_e = 4 \times 10^{18}\mathrm{cm}^{-3}$, as obtained from the target density measurements and the ionization degree of He, and assuming an average value of $r_\beta = 1\mu$m, we obtain $2.8 \leq K \leq 3.1$. This implies that for both energies we are well above the undulator limit and into the wiggler regime.

In Fig. 4, the experimental results for all the different gases are shown. In order to explore the role of the direct electron injection

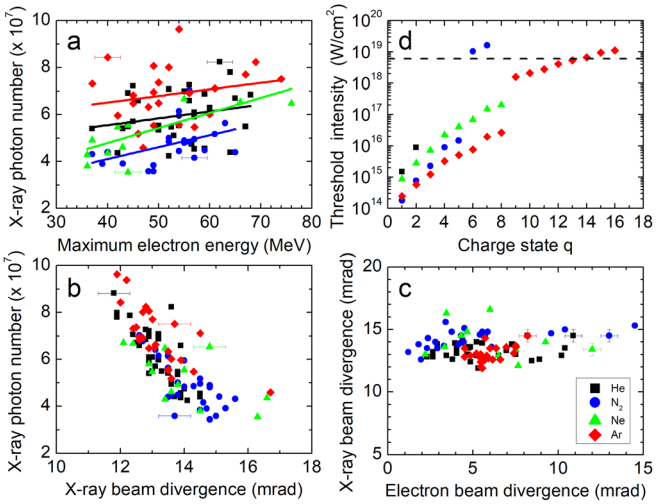

FIG. 4. (a)–(c) Experimental results for He, N_2, Ne, and Ar gases obtained with laser pulses having energy 570 mJ. Error bars for one data point in each gas are shown for clarity reasons. (a) X-ray photon number as a function of the maximum electron energy. The lines are linear fits to the data. (b) X-ray photon number as a function of the x-ray beam divergence. (c) X-ray beam divergence as a function of electron beam divergence. (d) Threshold laser intensity that is required for an ion to be stripped of q electrons. The dashed line indicates the intensity in use for the measurements.

inside the plasma bubble, the laser energy was limited to values significantly lower than the maximum energy delivered by the laser (1.3 J). For all the data presented hereafter in this article, the laser energy was maintained at the value of 570 mJ at the interaction region. Micrometric scale adjustments in the geometry of the laser beam focal area, necessary for a day-to-day operation of the optical system, were performed by moving an XYZ motorized stage that supported the gas jet. The aim of these adjustments was to achieve optimum betatron-type x-ray generation for each gas target and each backing pressure. Note that shadowgrams record the interaction region in shot-to-shot basis, and in combination with the interferometric measurements the critical parameters of interactions can be estimated for each shot.

In Fig. 4(a), the dependence of the x-ray photon number on the maximum electron energy is shown. In this figure, the presented data were selected having the same backing pressure of ∼40 bar and thus the same number of atoms within the interaction channel. Therefore, in this experiment, the role of the electrons contributing to the betatron-type x-rays efficiency could be examined. In Fig. 4(a), the data were fitted with linear fits to depict the x-rays efficiency trend for each gas element. Using He as the benchmark element for relative comparisons, it is clear that Ar corresponds to the highest efficiency of x-rays generation, while N_2 corresponds to the lowest. Neon seems to be in between these two limits and closer to He.

A phenomenological explanation for this behavior may rely on the number of electrons contributing to the LWFA process. In Fig. 4(d), we show the threshold laser intensity that is required for an ion to be stripped of q electrons, according to the over the barrier ionization (OBI) formula,[28] $I_{th,q}[\mathrm{W/cm^2}] = 4 \times 10^9 (1/q^2)(U_q[\mathrm{eV}])^4$, where U_q is the ionization potential for the q^{th} electron of an ion with charge $(q - 1)$. The ionization potentials necessary for the calculation were obtained from the NIST database.[29] The laser peak intensity, estimated to 6×10^{18} W/cm^2, was kept constant for this part of the experiments. This implies that He is fully doubly ionized well before the laser pulse peak, thus offering enough time for a clear plasma bubble formation since the evolution of the laser EM field occurs in a plasma environment free of rapid spatiotemporal electron density variations.[30] The latter favors the formation of the appropriate electron paths in phase space that lead adequate number of electrons, born at the leading edge of the laser pulse, to enter the bubble from the rear side following a closed orbit trajectory (self-injection).

The same reasoning seems to apply to N_2 as all of the 5 electrons of each N atom are ionized up to the leading edge of the laser pulse well before reaching the peak intensity. However, despite the large number of electrons, the resulted x-ray signal is less than in He. This could be attributed to the deviations from the optimum acceleration conditions due to the excess of electron density. The latter may distort the initiation time and the dynamical geometry of the bubble formation as well as the electron self-injection conditions inside the bubble due to the spatiotemporal rapid evolution of the electron density.[22]

As seen in Fig. 4(a), Ar gas presents the higher x-ray generation efficiency. Argon contributes free electrons to the plasma bubble formation both with self-injection of electrons born during the leading edge of the laser pulse as well as with electrons born after the peak of the laser pulse. Charge states 14th, 15th, and 16th of Ar and 6th and 7th for N cannot be reached through OBI with the peak intensity in use, indicated with a dashed line in Fig. 4(d). It should be emphasized here that even though OBI does not predict ionization for the above charge states of Ar and N, further ionization may proceed through a tunneling process.[19] The tunneling probability decreases rapidly with the difference between the threshold intensity for each charge state and the intensity in use here. From Fig. 4(d), it is evident that the tunneling probability should be considerably higher for the 14th Ar charge state compared to the 15th and 16th Ar charge states and to the 6th and 7th N charge states.

From the above analysis, the electrons resulting from the tunneling process in Ar^{13+} are those that are straightforwardly inserted inside the plasma bubble (ionization injection) since they are generated after the peak of the laser pulse and thus are not entrailed by the strong EM field of the laser peak. These electrons increase the number of electrons accelerated by the LWFA and consequently increase the x-rays generation efficiency for Ar at this laser intensity. In the literature, known practices for increasing the x-rays generation efficiency are the use of mixed gases, one of which contributes with electrons through self-injection (e.g., He) and the other with ionization injection (e.g., N_2)[31] and the down-ramp injection. The latter can be safely excluded for the reported results since the 10% modulation in plasma density, evident in Fig. 1(c), is not adequate for probing such mechanism.[32] Here, it is emphasized, that the important parameter for the efficient generation of the x-rays is not only the electron density of the plasma but also the number of electrons that enter the plasma wake and are further accelerated generating betatron-type x-rays. Thus, an alternative path toward the increase in the x-rays generation efficiency is to use a multi-electron gas, such as Ar, and appropriate laser peak intensity values.

Neon contributes to the plasma formation with eight electrons progressively added to the plasma formation up to the intensity of 2×10^{17} W/cm^2 which is at the leading edge of the pulse. Therefore, its behavior is closer to the He and N_2 cases (self-injection) than to Ar, as evident in Fig. 4(a).

In Fig. 4(b), the dependence of the x-ray photon number on the x-ray beam divergence is presented for all gases. The x-ray photon number decreases as a function of its angular divergence. This can be understood considering the dependence of the x-ray photon number N_γ on the Lorentz factor γ. For the wiggler regime, the dependence of the photon number on K is described[26] as $N_\gamma \sim K$ and thus scales as $N_\gamma \sim \gamma^{1/4}$. On the other hand, we have shown that the angular divergence scales as $\theta \sim \gamma^{-3/4}$. Therefore, higher γ values result in higher photon numbers, as shown in Fig. 3(a), corresponding to smaller angle divergence.

Finally, in Fig. 4(c) the dependence of the x-ray beam divergence on the electron beam divergence is shown. The x-ray divergence seems to be insensitive to the gas target. However, Ar presents a much narrower distribution in the electron beam divergence than the other gas targets. This implies better acceleration conditions, possibly owed to the direct ionization injection of electrons with zero kinetic energy inside the bubble.

In conclusion, betatron-type x-rays are generated using different gas targets in a LWFA scheme. The experimental setup allows for simultaneous recording of the x-ray beam characteristics along with relativistic electron beam in shot-to-shot basis. He gas target benchmark measurements were used to show the role of the laser peak intensity and the plasma channel length in the electron beam acceleration characteristics and simultaneously in the efficient betatron-type x-ray source. Additionally, the role of the multi-electron gas target in the betatron-type x-ray efficient generation is examined. These studies

propose an alternative path toward the increase in betatron-type x-ray efficiency by using multi-electron gas target and appropriate adjustment of the pumping laser peak intensity. This is a proof of principle finding that could be extended to a wide range of relativistic laser intensities and depends primarily on the selected gas target charge-state to attain the ionization injection scheme.

This research is co-financed by Greece and the European Union (European Social Fund-ESF) through the Operational Programme «Human Resources Development, Education and Lifelong Learning 2014–2020» in the context of the project "Development and optimization of the betatron-type radiation source induced by ulta-intense laser electromagnetic fields" (MIS No. 5048172). We would like to thank Dr. E. Clark for fruitful discussions and support, and Professor I. Fitilis and Mr. S. Petrakis for their engineering work on the laser system.

DATA AVAILABILITY

The data that support the findings of this study are available from the corresponding author upon reasonable request.

REFERENCES

[1]S. P. Mangles, C. Murphy, Z. Najmudin, A. G. R. Thomas, J. Collier, A. E. Dangor, E. Divall, P. Foster, J. Gallacher, C. Hooker *et al.*, "Monoenergetic beams of relativistic electrons from intense laser–plasma interactions," Nature **431**, 535–538 (2004).
[2]C. Geddes, C. Toth, J. Van Tilborg, E. Esarey, C. Schroeder, D. Bruhwiler, C. Nieter, J. Cary, and W. Leemans, "High-quality electron beams from a laser wakefield accelerator using plasma-channel guiding," Nature **431**, 538–541 (2004).
[3]J. Faure, Y. Glinec, A. Pukhov, S. Kiselev, S. Gordienko, E. Lefebvre, J.-P. Rousseau, F. Burgy, and V. Malka, "A laser–plasma accelerator producing monoenergetic electron beams," Nature **431**, 541–544 (2004).
[4]A. Rousse, K. T. Phuoc, R. Shah, A. Pukhov, E. Lefebvre, V. Malka, S. Kiselev, F. Burgy, J.-P. Rousseau, D. Umstadter *et al.*, "Production of a keV x-ray beam from synchrotron radiation in relativistic laser-plasma interaction," Phys. Rev. Lett. **93**, 135005 (2004).
[5]S. Kneip, C. McGuffey, J. L. Martins, S. Martins, C. Bellei, V. Chvykov, F. Dollar, R. Fonseca, C. Huntington, G. Kalintchenko *et al.*, "Bright spatially coherent synchrotron x-rays from a table-top source," Nat. Phys. **6**, 980–983 (2010).
[6]V. Malka, J. Faure, Y. A. Gauduel, E. Lefebvre, A. Rousse, and K. T. Phuoc, "Principles and applications of compact laser–plasma accelerators," Nat. Phys. **4**, 447–453 (2008).
[7]I. Tazes, J. Ong, O. Tesileanu, K. Tanaka, N. Papadogiannis, M. Tatarakis, and V. Dimitriou, "Target normal sheath acceleration and laser wakefield acceleration particle-in-cell simulations performance on CPU & GPU architectures for high-power laser systems," Plasma Phys. Controlled Fusion **62**, 094005 (2020).
[8]S. Kneip, C. McGuffey, F. Dollar, M. Bloom, V. Chvykov, G. Kalintchenko, K. Krushelnick, A. Maksimchuk, S. Mangles, T. Matsuoka *et al.*, "X-ray phase contrast imaging of biological specimens with femtosecond pulses of betatron radiation from a compact laser plasma wakefield accelerator," Appl. Phys. Lett. **99**, 093701 (2011).
[9]J. Cole, J. Wood, N. Lopes, K. Poder, R. Abel, S. Alatabi, J. Bryant, A. Jin, S. Kneip, K. Mecseki *et al.*, "Tomography of human trabecular bone with a laser-wakefield driven x-ray source," Plasma Phys. Controlled Fusion **58**, 014008 (2016).
[10]F. Albert and A. G. Thomas, "Applications of laser wakefield accelerator-based light sources," Plasma Phys. Controlled Fusion **58**, 103001 (2016).
[11]J. M. Cole, D. R. Symes, N. C. Lopes, J. C. Wood, K. Poder, S. Alatabi, S. W. Botchway, P. S. Foster, S. Gratton, S. Johnson *et al.*, "High-resolution μct of a mouse embryo using a compact laser-driven x-ray betatron source," Proc. Natl. Acad. Sci. U. S. A. **115**, 6335–6340 (2018).
[12]J. C. Wood, D. Chapman, K. Poder, N. Lopes, M. Rutherford, T. White, F. Albert, K. Behm, N. Booth, J. Bryant *et al.*, "Ultrafast Imaging of laser driven shock waves using betatron x-rays from a laser wakefield accelerator," Sci. Rep. **8**, 1–10 (2018).
[13]A. E. Hussein, N. Senabulya, Y. Ma, M. Streeter, B. Kettle, S. J. Dann, F. Albert, N. Bourgeois, S. Cipiccia, J. M. Cole *et al.*, "Laser-wakefield accelerators for high-resolution x-ray imaging of complex microstructures," Sci. Rep. **9**, 1–13 (2019).
[14]S. Corde, K. T. Phuoc, R. Fitour, J. Faure, A. Tafzi, J.-P. Goddet, V. Malka, and A. Rousse, "Controlled betatron x-ray radiation from tunable optically injected electrons," Phys. Rev. Lett. **107**, 255003 (2011).
[15]F. Albert, B. Pollock, J. Shaw, K. Marsh, Y.-H. Chen, D. Alessi, J. Ralph, P. Michel, A. Pak, C. Clayton *et al.*, "Betatron x-ray production in mixed gases," Proc. SPIE **8779**, 87791Q (2013).
[16]K. Huang, D. Li, W. Yan, M. Li, M. Tao, Z. Chen, X. Ge, F. Liu, Y. Ma, J. Zhao *et al.*, "Simultaneous generation of quasi-monoenergetic electron and betatron x-rays from nitrogen gas via ionization injection," Appl. Phys. Lett. **105**, 204101 (2014).
[17]K. Behm, T. Zhao, J. Cole, A. Maksimchuk, S. Mangles, J. Nees, J. Wood, V. Yanovsky, K. Krushelnick, and A. Thomas, "Ionization injection effects in x-ray spectra generated by betatron oscillations in a laser wakefield accelerator," Plasma Phys. Controlled Fusion **58**, 055012 (2016).
[18]C. McGuffey, A. Thomas, W. Schumaker, T. Matsuoka, V. Chvykov, F. Dollar, G. Kalintchenko, V. Yanovsky, A. Maksimchuk, K. Krushelnick *et al.*, "Ionization induced trapping in a laser wakefield accelerator," Phys. Rev. Lett. **104**, 025004 (2010).
[19]M. Chen, E. Esarey, C. Schroeder, C. Geddes, and W. Leemans, "Theory of ionization-induced trapping in laser-plasma accelerators," Phys. Plasmas **19**, 033101 (2012).
[20]E. Guillaume, A. Döpp, C. Thaury, A. Lifschitz, J.-P. Goddet, A. Tafzi, F. Sylla, G. Iaquanello, T. Lefrou, P. Rousseau *et al.*, "Physics of fully-loaded laser-plasma accelerators," Phys. Rev. Spec. Top.-Accel. Beams **18**, 061301 (2015).
[21]K. Huang, Y. Li, D. Li, L. Chen, M. Tao, Y. Ma, J. Zhao, M. Li, M. Chen, M. Mirzaie *et al.*, "Resonantly enhanced betatron hard x-rays from ionization injected electrons in a laser plasma accelerator," Sci. Rep. **6**, 1–8 (2016).
[22]A. Pak, K. Marsh, S. Martins, W. Lu, W. Mori, and C. Joshi, "Injection and trapping of tunnel-ionized electrons into laser-produced wakes," Phys. Rev. Lett. **104**, 025003 (2010).
[23]G. Andrianaki, A. Grigoriadis, E. P. Benis, and N. A. Papadogiannis, "Pointing characteristics of x-rays generated by relativistic electron acceleration via 45 tw fs laser-he plasma," in *The 22nd International Conference on Ultrafast Phenomena* (Optical Society of America, 2020).
[24]Z. Najmudin, K. Krushelnick, M. Tatarakis, E. Clark, C. Danson, V. Malka, D. Neely, M. Santala, and A. Dangor, "The effect of high intensity laser propagation instabilities on channel formation in underdense plasmas," Phys. Plasmas **10**, 438–442 (2003).
[25]B. L. Henke, E. M. Gullikson, and J. C. Davis, "X-ray interactions: Photoabsorption, scattering, transmission, and reflection at e= 50–30,000 ev, z = 1–92," At. Data Nucl. Data Tables **54**, 181–342 (1993).
[26]S. Corde, K. T. Phuoc, G. Lambert, R. Fitour, V. Malka, A. Rousse, A. Beck, and E. Lefebvre, "Femtosecond x rays from laser-plasma accelerators," Rev. Mod. Phys. **85**(1), 1 (2013).
[27]K. T. Phuoc, F. Burgy, J.-P. Rousseau, V. Malka, A. Rousse, R. Shah, D. Umstadter, A. Pukhov, and S. Kiselev, "Laser based synchrotron radiation," Phys. Plasmas **12**, 023101 (2005).
[28]E. E. Fill, "Focusing limits of ultrashort laser pulses: Analytical theory," J. Opt. Soc. Am. B **11**, 2241–2245 (1994).
[29]See https://www.nist.gov/ for ionization potentials of atomic ions.
[30]J. C. Wood, "Betatron radiation from laser wakefield accelerators and its applications," Ph.D. thesis (Imperial College London, 2016).
[31]V. Tomkus, V. Girdauskas, J. Dudutis, P. Gečys, V. Stankevič, G. Račiukaitis, I. G. González, D. Guénot, J. B. Svensson, A. Persson *et al.*, "Laser wakefield accelerated electron beams and betatron radiation from multijet gas targets," Sci. Rep. **10**, 1–17 (2020).
[32]C. G. R. Geddes, K. Nakamura, G. R. Plateau, C. Toth, E. Cormier-Michel, E. Esarey, C. B. Schroeder, J. R. Cary, and W. P. Leemans, "Plasma-density-gradient injection of low absolute-momentum-spread electron bunches," Phys. Rev. Lett. **100**, 215004 (2008).